The effects of thermal treatment under argon–oxygen ambient on the microstructure and optical properties of DC sputtered Cr thin films for selective solar absorbers applications

J. J. Tibaijuka[1,*] , J. S. Nyarige[2], M. Diale[2], N. R. Mlyuka[1], and M. E. Samiji[1]

[1] Physics Department, University of Dar es Salaam, P.O Box 35063, Dar es Salaam, Tanzania
[2] Physics Department, University of Pretoria, Private Bag X20, Hatfield 0028, South Africa

ABSTRACT

This work investigated the effect of thermal treatment of as-deposited chromium (Cr) thin films in a vacuum and argon/oxygen ambient for effective deposition of spectral selective solar absorber multilayer films. The DC sputtered Cr thin films were thermally exposed at different temperatures in a controlled argon/oxygen environment. Both as-deposited films and those thermally treated in vacuum and in oxygen–argon ambient revealed a weak XRD diffraction peak at $2\theta \approx 44.3°$ corresponding to (110) plane of BCC structure of Cr metal. Raman analysis revealed one peak at $846\ cm^{-1}$ corresponding to Cr–O vibration bonds for films thermally treated at 300 °C in a vacuum and 150 °C and 300 °C in argon–oxygen ambient. As determined by AFM and FE-SEM, surface roughness decreased with temperature increase for films thermally treated in a vacuum. Besides, a mixed trend in the evolution of surface roughness was observed for films thermally treated in argon/oxygen ambient. The average spectral transmittance for samples thermally treated in a vacuum decreased with an increase in temperature; however, the samples thermally treated in an argon–oxygen environment exhibited an increasing trend in average spectral transmittance with the increase in temperature. The results clearly show that post-deposition processing at elevated temperatures, particularly in argon–oxygen ambient, influences the structural and optical properties of prior-deposited Cr thin films. This should be considered when designing and depositing multi-layered dielectric/Cr spectral selective solar absorber films.

Address correspondence to E-mail: jtibaijuka14@gmail.com; justine.tibaijuka@udsm.ac.tz

🌲 Springer

1 Introduction

Demands for spectral selective solar materials that can withstand high operating temperatures while satisfying the spectral solar selectivity conditions in solar thermal conversion technology are driving significant research interest [1–5]. Besides being of interest for several applications such as photo masks, reticules and pinhole on glass substrate integrated circuits and optical beam splitters [6–8], chromium thin films have been researched for selective solar absorber applications [9, 10]. The interest in Cr thin films is due to their properties that includes good adhesion, high melting point, high wear and corrosion resistance, and high thermal conductivity [11, 12]. These material properties are essential for a broad and diverse range of high-temperature applications. Furthermore, intrinsic spectral selectivity in Cr thin films can be tuned to suit various applications, thus making it a potential for the novel design of selective solar absorbers [8].

Some of the ways in which spectral selectivity in Cr thin films can be tuned include appropriate control of the deposition conditions and use of antireflection coatings in a multilayer structure such as dielectric metal dielectric (DMD) designs utilizing two dielectrics with the metal layer between them. Cr, among other metals, has shown great potential in spectral selectivity when sandwiched between dielectric materials such as Cr_2O_3 [10, 13].

Different deposition methods have been employed to explore the microstructure and optical properties of Cr and DMD coatings that incorporate metallic Cr thin films. These include chemical vapor deposition, DLI-MOCVD, pulsed laser deposition, spray pyrolysis, sol–gel spin coating, thermal evaporation, and sputtering, to mention few [14–16]. Among these methods, DC sputtering is versatile and suitable for large area deposition due to its relatively high deposition rate and being environmental friendly [17]. Again, most of the thin films produced by this method have high-quality uniform films with exceptional physical and optical properties [18, 19].

For multilayer-based spectral selective solar absorbers, the interface structure and composition are vital factors controlling the performance and reliability of the devices [20]. The dielectrics usually absorb well in the visible wavelength range, and the underlying metallic layer (Cr) helps to reflect the infrared wavelength and reduce the emissivity. Thus,

the quality and stability of the mid-metal play a decisive role in influencing the overall performance of the selective coating. During post-deposition processing at elevated temperatures, inter-diffusion and oxidation from introduced gases and residual oxygen could change the composition and structure of the film interfaces if not properly optimized [6, 21]. When depositing the top dielectric in a DMD multilayer stack through DC reactive sputtering at elevated temperature for example, there is a possibility of changing properties of the metal layer due to the introduced argon–oxygen gases and the subsequent heating. Besides improving the film properties, heating is reported to cause thermal fatigue damage and the expansion mismatch that creates maximum compressive stress at the interface [22]. Furthermore, subject to heating and the introduction of sputtering and reactive gas, the film interface structure and composition of the existing film could change and, consequently, the performance and the reliability of the thin film device. Nevertheless, the effect of these changes to the microstructure and optical properties of Cr metallic layer remains an open research question. Thus, for effective deposition of Cr-based multilayer selective absorbers, it is essential to have a good understanding of the optical and structural changes that may evolve due to the effect of sputtering and reactive gases and thermal heating during deposition of the dielectric layer. With this concern, this study conducted a systematic investigation to determine how exposure of the as-deposited Cr films to elevated temperatures in vacuum and in argon–oxygen ambient affects its microstructure and optical properties.

2 Experiment

2.1 Sample preparation

The deposition of ∼ 32 ± 0.5 nm thick Cr thin films onto 3.5 cm × 2.5 cm × 1 mm Soda lime glass (SLG) substrates was achieved at room temperature by DC magnetron sputtering of high-purity Cr target (99.99%) commercially acquired from Plasmaterials Inc. The deposition and heat treatment were done using the BALZERS BAE 250 coating unit. Before deposition, SLG substrates were first cleaned ultrasonically then rinsed in distilled water and ethanol, before being suspended in ethanol vapor. The

sputtering chamber was first evacuated to a base pressure of 6.8×10^{-6} mbar using a turbo-molecular pump backed up with a rotary pump before initiating sputtering at a power of 25 W and working pressure of $5.0 \times \times 10^{-3}$ mbar using high-purity argon gas (99.99%) flowing at a rate of 15 SCCM as ascribed in Tibaijuka et al. [15]. The schematic illustration showing the deposition of Cr on G glass is as shown in Fig. 1. Thermal treatment of the as-deposited films was done in vacuum and in argon–oxygen (15:8.5) ambient using the BAE 250 built-in system heater at a fixed time interval of 30 min and temperature that was varied between 100 and 300 °C.

2.2 Sample characterization

The thickness of the films was determined using the Alpha Step surface profiler by measuring the step created using a Teflon tape stacked on a substrate before deposition. The surface morphology of the films was investigated using Zeiss Crossbeam 540 Field Emission-Scanning Electron Microscopy (FE-SEM) operating at 2 kV and a Nanoscope IIIA atomic force microscope in tapping mode. The grains distribution and surface roughness were analyzed from the SEM and AFM images using ImageJ2 software [23] and WSxM software (version 4.0) [24], respectively. The structural properties of the films were determined using an X-ray Diffractometer (XRD) in which Cu K-alpha radiation of 0.1504 nm wavelength

Fig. 1 Schematic diagram of the sputtering chamber used for fabrication and treatment of Cr thin films

and a scanning speed of 0.050° per minute for the 2θ ranging from 20° to 70° were used. The resulting phases were confirmed with the help of reference PDF data from the ICDD database. The solar transmittance (T_{sol}) and reflectance (R_{sol}) spectra in the wavelength ranging from 250 to 2500 nm were measured using Perkin Elmer Lambda 1050 + UV/VIS/NIR spectrophotometer. The optical constants were determined by fitting theoretical and measured transmittance and reflectance data using Scout software (2.4, WTheiss Hardware and Software) as ascribed by Khelifa et al. [10].

3 Results and discussions

3.1 Structural analysis

The structural properties of as-deposited and thermal-treated chromium films were examined using an X-ray diffraction (XRD) and Raman spectroscopy system. As depicted in Fig. 2, both as-deposited and thermally treated samples in the vacuum and oxygen–argon ambient revealed the weak diffraction peak at $2\theta \approx 44.3°$, corresponding to (110) plane of Cr metal BCC structure as per the Joint Committee of Powder Diffraction Standards (JCPDS) PDF No.06-0694. There were no chromium oxide peaks revealed in XRD diffractograms. However, Raman studies shown in Fig. 3 revealed one peak at 846 cm^{-1} for films thermally treated at 300 °C in a vacuum and those treated at a temperature of 150 °C and 300 °C in argon–oxygen ambient. The aforementioned peak was associated to Cr–O stretching modes [25]. Besides, the observed Raman peak at 934 cm^{-1} can be attributed to arises from components within the glass substrate [26]. The formation of Cr–O is triggered by the reaction of Cr films with the introduced oxygen gas and the residual oxygen from the sputtering chamber. The grain size was estimated using the basic Debye–Scherrer formula (Eq. 1) as ascribed by Ollotu et al. [19] upon which the full width at half maximum (FWHM) was determined by fitting the diffractgrams with the help of Originlab (Pro) 2018 software. On the other hand, the microstrain was estimated using Eq. 2 as ascribed by Kumar et al. [27].
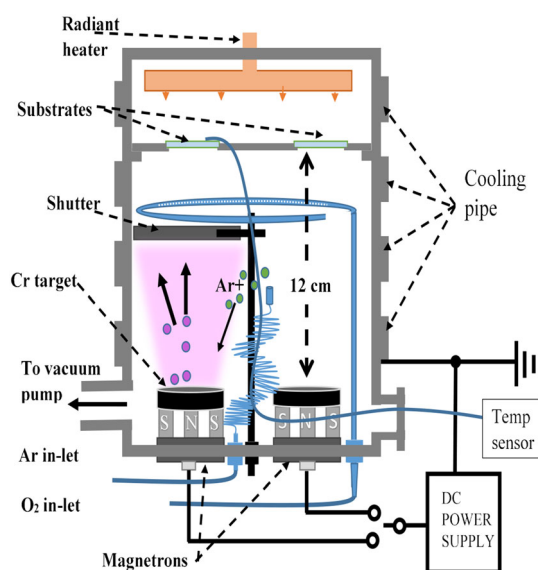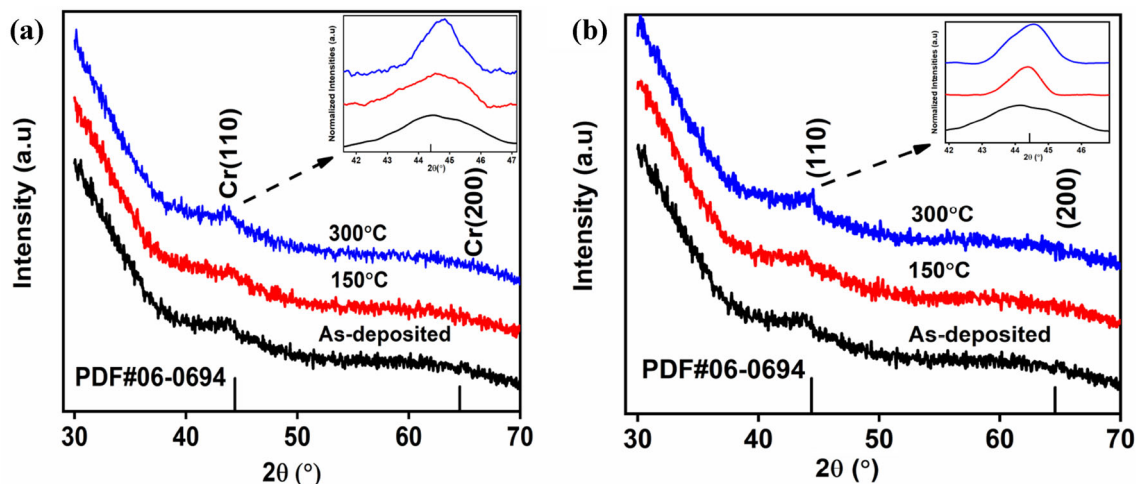
Fig. 2 XRD spectra of Cr thin films thermally treated at different temperatures in vacuum (**a**) and argon/oxygen ambient (**b**)
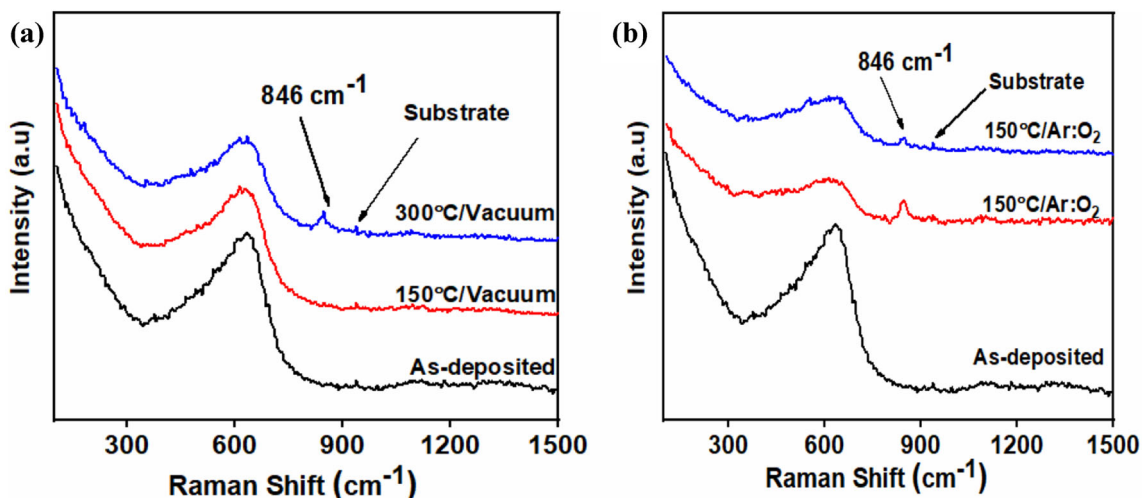

Fig. 3 Raman spectra of Chromium thin films thermally treated at different temperatures in **a** vacuum and **b** Argon–Oxygen ambient

$$D = \frac{K\lambda}{\beta \cos\theta} \quad (1)$$

$$\varepsilon = \frac{\beta \cos\theta}{4} \quad (2)$$

where D, λ, β, ε θ, and K stand for crystallite size, XRD radiation wavelength, FWHM of a dominant peak, the micro-strain, Bragg angle and the Scherrer constant, respectively. In this study, $K = 0.94$ was used.

It can be observed that for films treated in a vacuum, the average crystallite size was in the range of 3.3–6.4 nm and increased with the increase of temperature (Fig. 2 inset), whereas the microstrain

estimated from the crystallite size decreased with temperature as summarized in Table 1. The observed change may be contributed by the decrease of grain boundaries with temperature and the relief of residual stress in the films due to thermal expansion with an increase in temperature [28, 29]. The decrease of microstrain value with an increase in crystallite size is also reported by Naveena et al. [30], Baturay et al. [31], and Kumar et al. [27] who associated it with the reduction of lattice imperfections and improvement of film quality. Besides, the average crystallite size was in the range of 3.3–8.6 nm for the films thermally treated in argon oxygen ambient; however, no clear trend was observed on the variation of average

Table 1 Full Width at Half Maximum (FWHM), peak positions (2θ), the crystallite size (D), and macrostrain (ε) for Chromium films thermally treated at different temperatures in vacuum and in argon–oxygen ambient

Sample ID	2θ (°)	FWHM (°)	D(nm) ± 0.1 (nm)	(hkl)	$\varepsilon \times 10^{-2}$
As deposited	44.26	2.78	3.2	(1 1 0)	3.04
150 °C/Vacuum	44.29	2.10	4.2	(1 1 0)	2.29
300 °C/Vacuum	44.32	1.39	6.4	(1 1 0)	1.52
150 °C/Ar:O_2	44.32	1.03	8.6	(1 1 0)	1.12
300 °C/ Ar:O_2	44.37	1.35	6.6	(1 1 0)	1.46

crystallize size and there corresponding microstrain. It is evident from these results that the high temperature and the introduced argon–oxygen gas during deposition of the subsequent dielectric layer in the Cr-based multilayer spectral selective films can significantly influence the structure of the prior deposited Cr.

3.2 Surface morphology

The surface morphology of the as-deposited and thermal treated films was examined using FE-SEM and AFM. Figures 4 and 5 show the SEM micrograph of Cr thin films of both as-deposited and thermally treated films in a vacuum and argon–oxygen ambient. The SEM micrographs reveal an increase in clustered grain size with an increase in temperature for film thermally treated in a vacuum. Similarly, the same trend was observed in films treated in argon–oxygen ambient.

The analysis of the grains done by Gaussian fitting of statistical distribution as ascribed by Kumar et al. [32], revealed nearly normal distribution of grains for the as-deposited (Figs. 4d, 5d) and left skewed as the temperature increased in both vacuum and argon/oxygen ambient. The average grain size ranging between 5.9–8.1 nm and 6.1–8.1 nm was recorded for films thermally treated in vacuum and argon/oxygen atmosphere, respectively. Moreover, the films treated in an argon–oxygen environment had relatively larger average grain size than those thermally treated in a vacuum environment (Fig. 6). Unlike the as-deposited films, the films treated at 150 °C formed rods-like structures which disappeared when treatment temperature increased to 300 °C. It is worth mentioning that the grains get less clustered and become nearly spherical in shape when films are subjected to heat treatment above 300 °C [33]. These results again

confirm the influence of heat and the introduced argon–oxygen gas in the deposition chamber on the morphology of prior-deposited Cr-films before deposition the subsequent layer.

Figures 7 and 8 present two-dimensional (2D) and three-dimensional (3D) AFM topographical images of the as-deposited chromium thin films thermally treated at different temperatures in vacuum and argon/oxygen ambient. AFM micrographs reveal the small cluster of grains for both chromium films, thermally treated in vacuum and argon/oxygen conditions (Figs. 7a–b, 8a–b). To visualize the effect of thermal treatment on the surface topography in both conditions, the AFM images were processed for surface roughness using WSxM software (version 4.0). It can be observed that for Cr films thermally treated in a vacuum, the average roughness (R_a) and the root-mean-square roughness (R_{rms}) decreased from 6.1 to 2.0 nm and 7.9 to 2.5 nm, respectively (Fig. 9a; Table 2). The decrease in roughness observed was associated with the improvement of homogeneity of the film due to island coalescence with the increase in temperatures [34]. Conversely, for Cr films thermally treated in argon/oxygen ambient, R_a and R_{rms} values first decreased from 6.1 to 2.0 nm and 7.9 to 2.7 nm and then increased to 3.7 nm and 5.0 nm, respectively, when temperature increased further (Fig. 9b; Table 2).

To analyze further the effect of thermal treatment on film topography, the skewness and kurtosis parameters which are vital in determining the symmetry and sharpness or peakedness of surface height distribution [15, 35] were estimated from the surface height distribution histograms of the samples (Figs. 7g–i, 8g–i). It can be observed that, for Cr films thermally treated in a vacuum, the skewness values decreased from 4.5 to 0.3 with the increase in temperature indicating the shifting of skewed
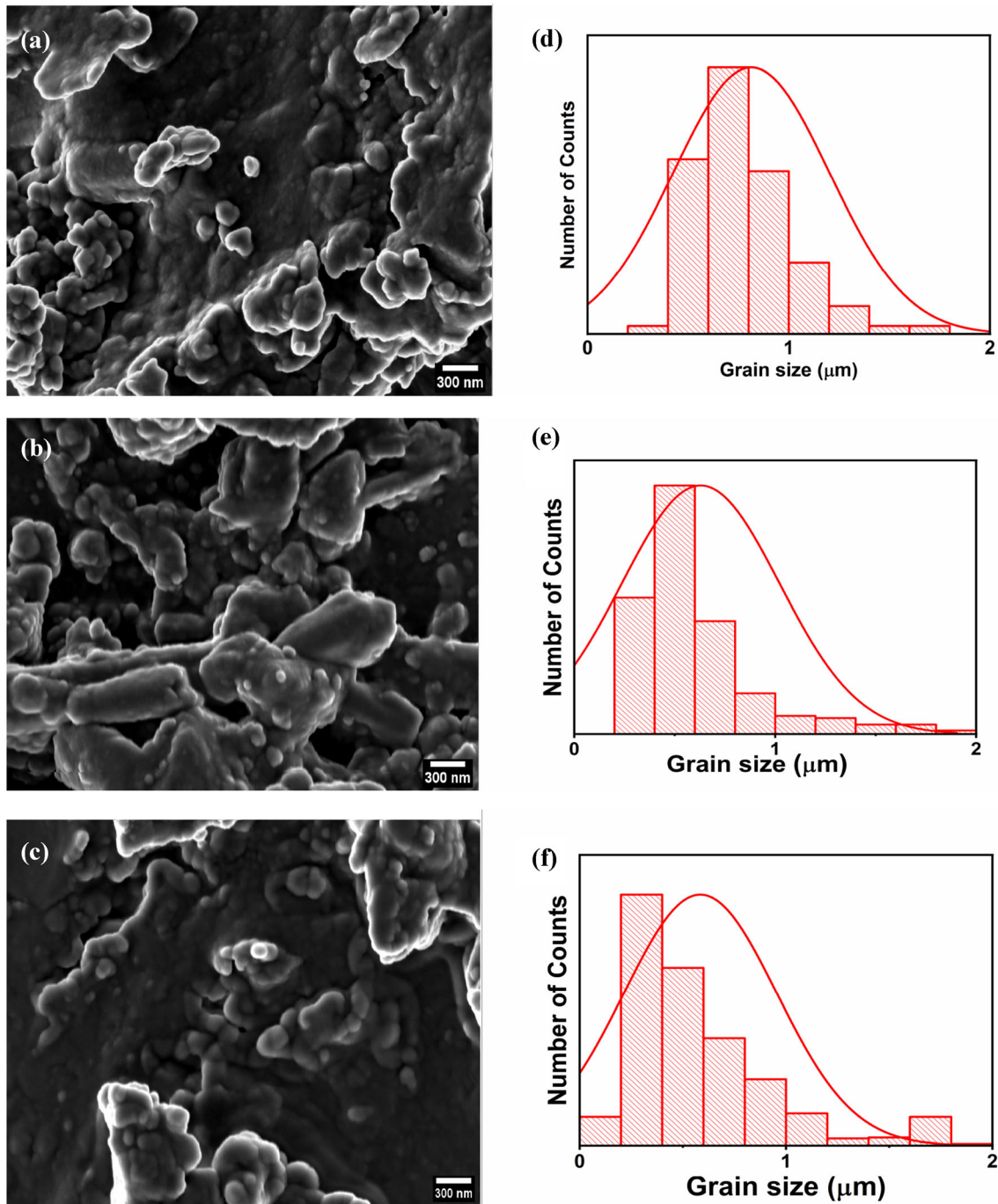
Fig. 4 FE-SEM images of Chromium thin films thermally treated in vacuum at different temperatures: **a, d** As-deposited **b, e** 150 °C/Vacuum, **c, f** 300 °C/Vacuum

distribution toward the left (Table 2; Fig. 8b). This was attributed to the decrease in heights above the average and an increase of valleys with increase in temperature [15, 36]. Moreover, the kurtosis value increased from 0.93 to 3.1, indicating the increase in narrowness and sharpness of surface height
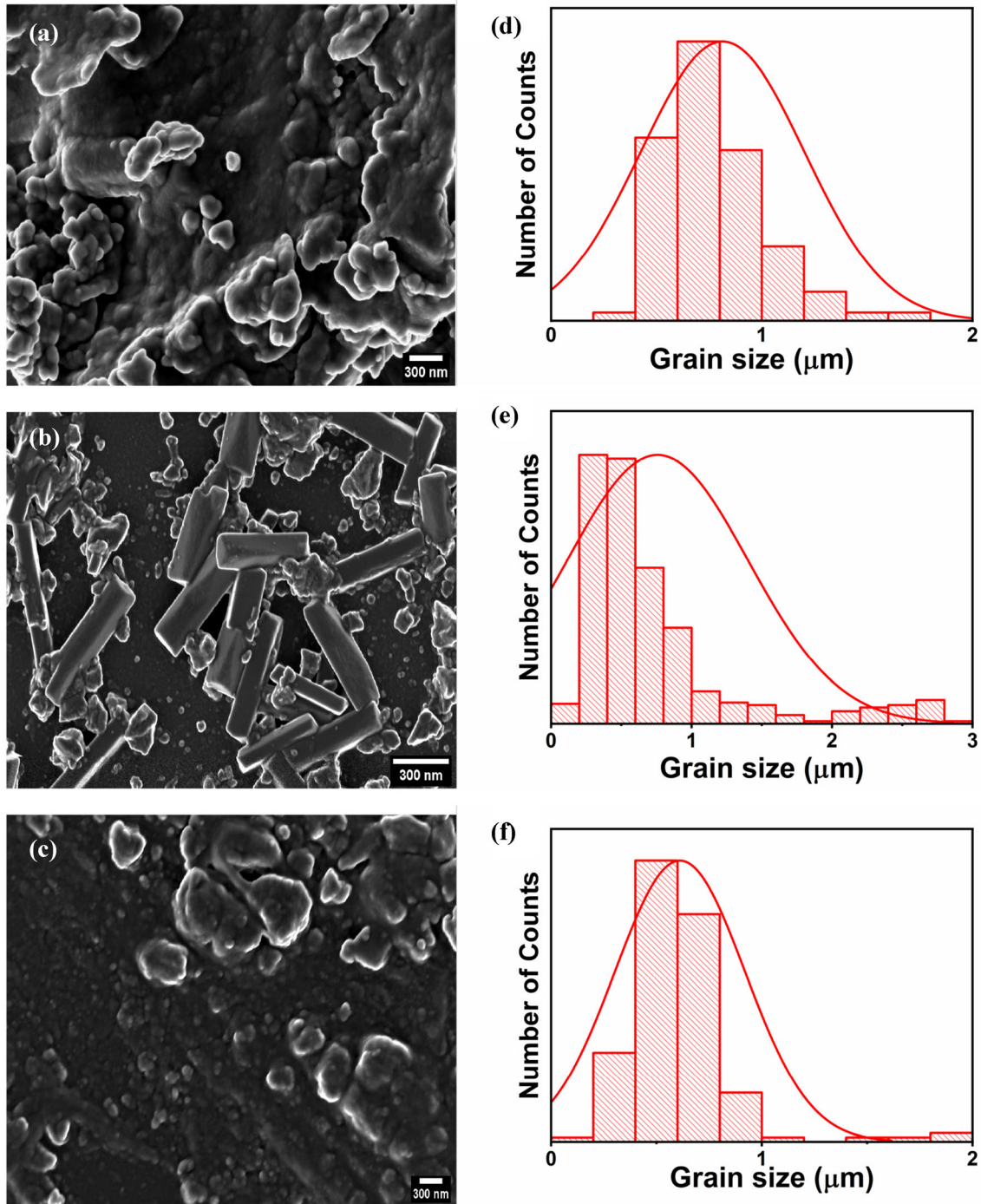
Fig. 5 SEM images and their corresponding grain size distributions of Chromium thin films thermally exposed in argon–oxygen ambient at different temperatures **a**, **d** As-deposited, **b**, **e** 150 °C/ Ar:O_2, **c**, **f** 300 °C/Ar:O_2
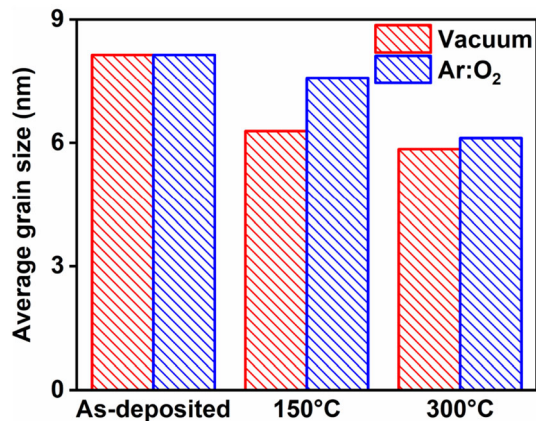
Fig. 6 Average grain size of films thermally treated in vacuum and in argon/oxygen ambient

distributions of Cr films with the increase in temperature. Besides, for Cr films thermally treated in argon/oxygen ambient, the skewness values ranged between 1.9 and 4.5, showing a substantial height distribution above the average (Table 2; Fig. 9b). Similarly, the Kurtosis values for films treated in argon/oxygen ambient increased from 0.93 to 29.6 with an increase in temperature indicating the shifting distribution toward the positive values which signify the increase in narrowness and sharpness of surface height distributions of Cr films with an increase in temperature [36].

3.3 Optical properties

Figure 10 shows the transmittance and reflectance spectra of Cr films thermally treated in vacuum and argon/oxygen ambient, respectively. It can be seen that all films exhibited a relatively high transmittance in the infrared region compared to the visible region in a solar spectrum. To observe the variation in solar transmittances, the films' average solar transmittances, T_{sol}, were computed using Eq. (3) as described by Ollotu et al. [37] utilizing Air Mass 1.5 solar irradiance $G(\lambda)$.

$$T_{sol} = \frac{\sum_{250}^{2500} T(\lambda)G(\lambda)}{\sum_{250}^{2500} G(\lambda)} \tag{3}$$

The average transmittance ranged between 22 and 36%, and decreased with temperature for Cr films thermally treated in vacuum and increased with

temperature for Cr films thermally treated in argon/oxygen ambient. On the other hand, the general increasing trend of reflectance with temperature was observed for Cr films thermally treated in the vacuum. However, a decreasing trend of reflectance with the increase in temperature was observed in argon/oxygen ambient. It is worth mentioning that optical transmittance decrease during heat treatment is generally associated with either increase in crystallinity leading to improvement in reflectance or an increase in roughness resulting in much scattering of light [38]. In the present case, it can be concluded that the decrease in transmittance for films thermally treated in vacuum was due to an increase in crystallinity since the roughness was decreasing, as explained elsewhere in Table 2. Besides, the observed increase in average transmittance in films thermally treated in argon–oxygen ambient (Fig. 10a inset) is most likely due to the oxidation of surface Cr metal into chromium oxide, which usually has higher transmittance than the reflective Cr metal. Conversely, all films exhibited high reflectance in the visible region and decreased reflectance in the near-infrared region. In addition, it can be seen that solar absorbance improved with the increase in temperature for films thermally treated in vacuum while the solar absorbance decreased with the increase in temperature for films thermally treated in argon–oxygen environment (Fig. 10e, f). With these results, it worth to say that thermal treatment of Cr films in vacuum can improve the solar absorbance with the possibility of deteriorating it when exposed in argon–oxygen environment before depositing the subsequent dielectric layer.

Figure 11a and b shows the refractive index, n and their corresponding extinction coefficient, k, determined through the fitting of theoretical and measured transmittance and reflectance data using Scout software. In both cases, the values of n ranged between 2.5 and 3.5, and the k values varied between 1.5 and 2.4 in the visible near-infrared spectral range signifying the metallic behavior of Cr metal [15]. Furthermore, the refractive index increased with the increase of temperature in the visible spectrum while the extinction coefficient dropped with temperature in the same region for thermally treated films in a vacuum (Fig. 11a). On the other hand, the films
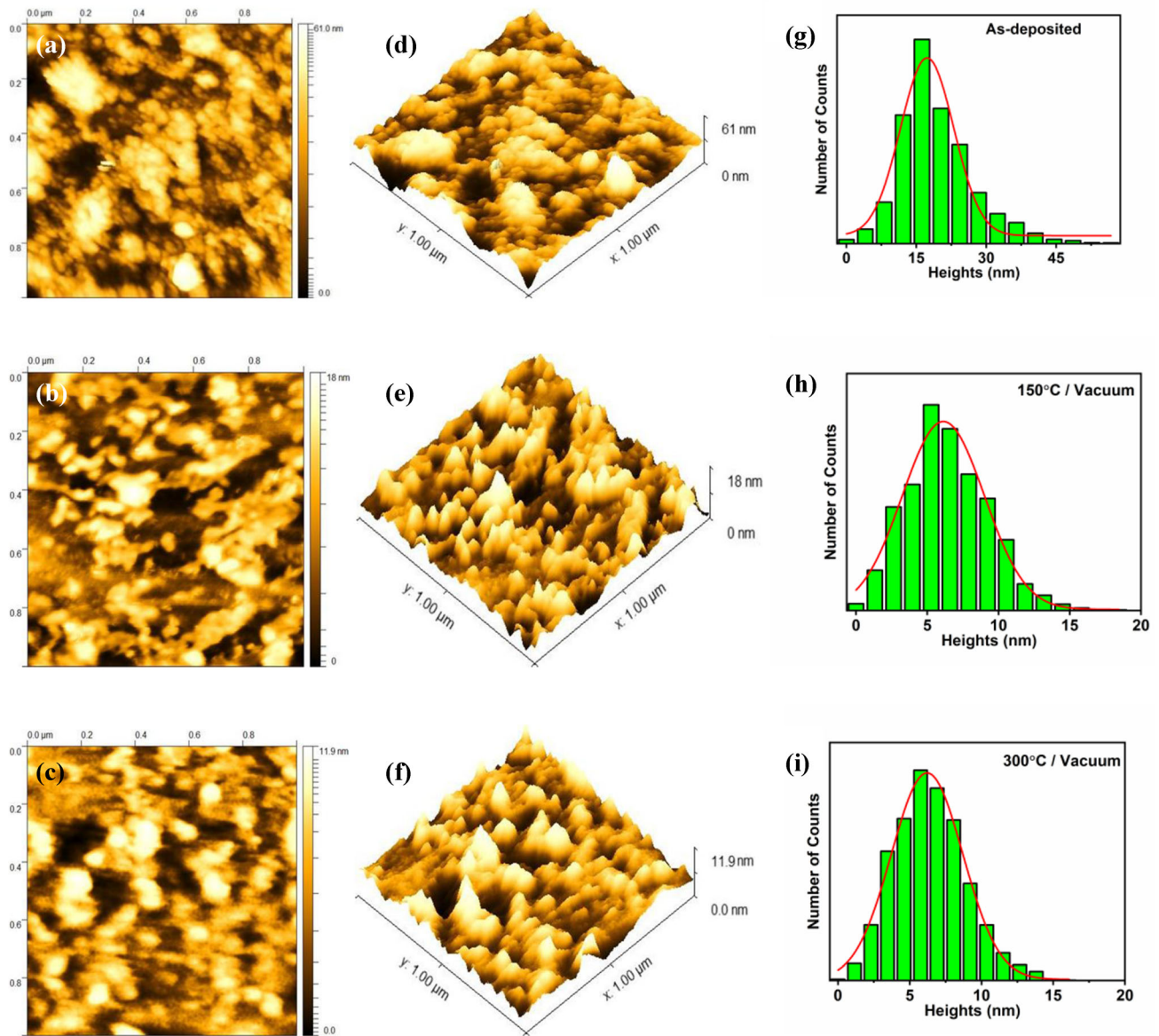th-
h-

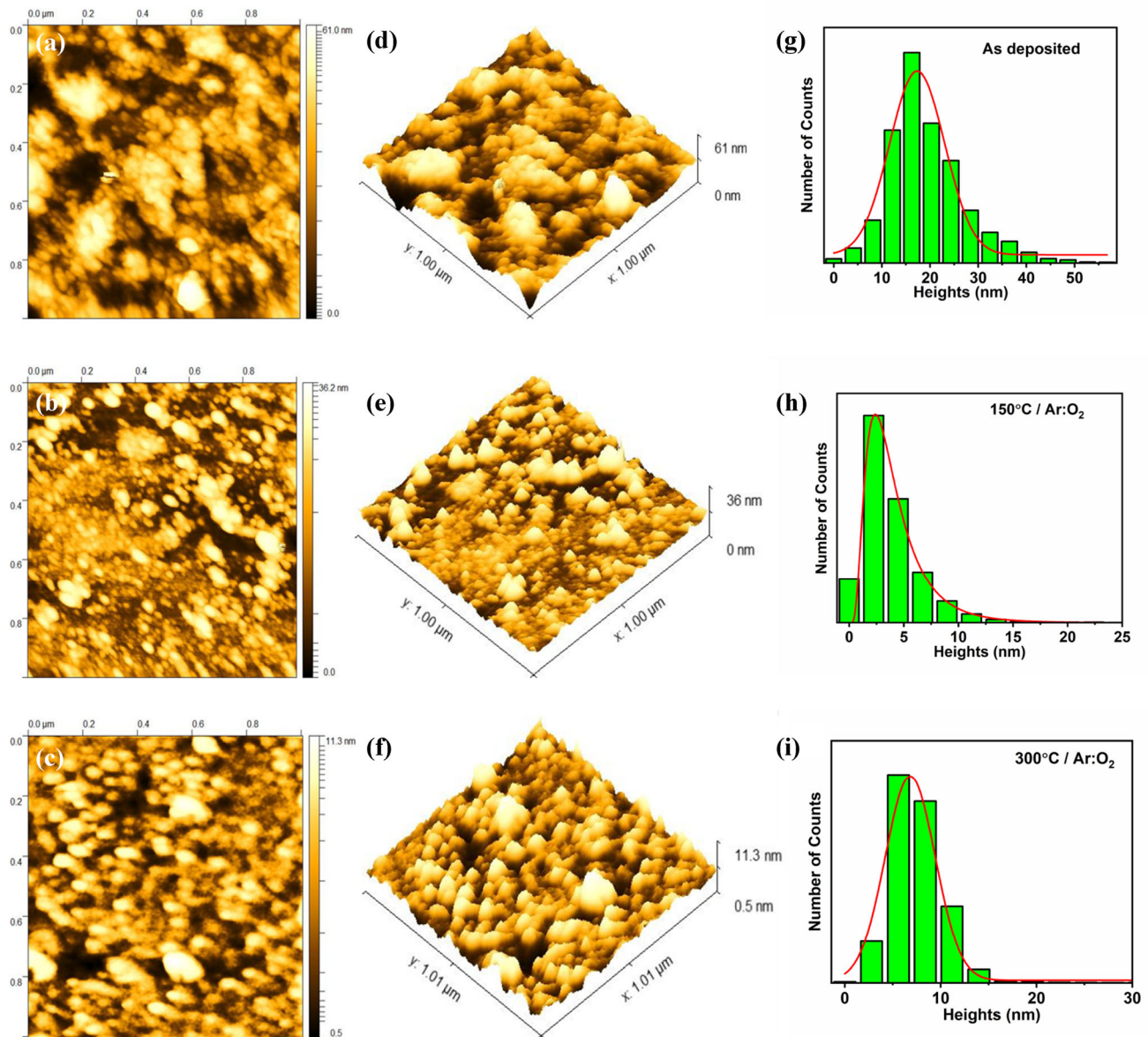**Fig. 7** 2D and 3D AFM images with corresponding height distributions for Cr films thermally exposed at different temperatures: (**a**, **d**, **g**)—as-deposited, (**b**, **e**, **h**) -150 °C/ Vacuum and (**c**, **f**, **i**) -300 °C/Vacuum

ermally treated in argon–oxygen environment, their refractive index decreased with the increase in temperature while the extinction coefficient dropped with temperature in the near-infrared region (Fig. 11b). This can be attributed to fact that films became denser with the increase in temperature when thermally treated in a vacuum environment and less denser with the increase in temperature when thermally treated in the argon–oxygen environment.

Fig. 8 2D and 3D AFM images with corresponding height distributions for Cr films thermally exposed at different temperatures in argon–oxygen ambient: as-deposited (**a, d, g**), 150 °C/ Ar:O$_2$ (**b, e, h**) and 300 °C/ Ar:O$_2$ (**c, f, i**)

4   Conclusions

Cr thin films were successfully deposited by DC sputtering followed by subsequent thermal treatment at different temperatures in vacuum and in argon–oxygen ambient. XRD analysis of the as-deposited and the treated films revealed a weak diffraction peak at $2\theta \approx 44.3°$, assigned to (110) planes of the BCC Chromium structure. Raman analysis revealed one peak at 846 cm^{-1} attributed to Cr–O stretching modes when the films were thermally treated at 300 °C in vacuum and at temperatures of 150 °C and 300 °C in argon–oxygen ambient. AFM and SEM analysis showed a decrease in surface roughness with
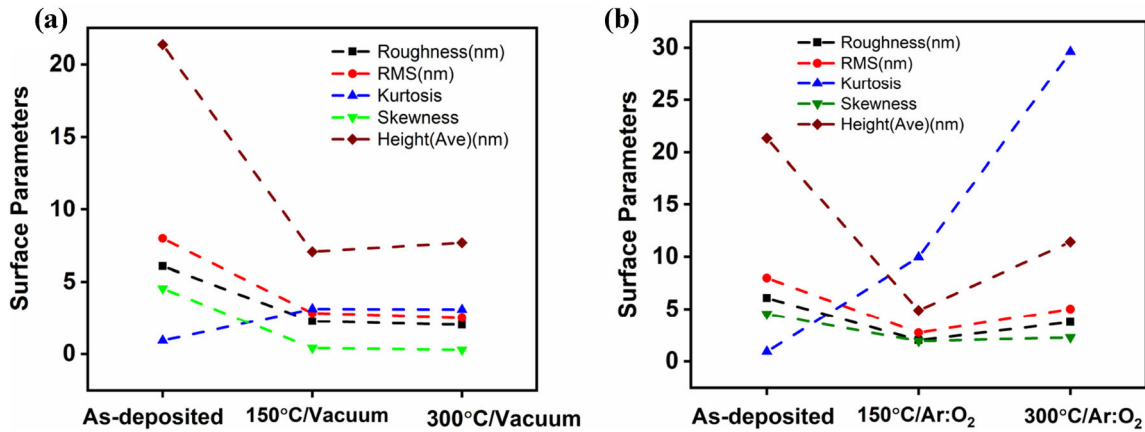
Fig. 9 AFM surface parameters for Cr films thermally treated at different temperatures in **a** Vacuum **b** Argon–Oxygen ambient

Table 2 AFM surface parameters for Cr films thermally treated at different temperatures in a vacuum and Ar:O_2 ambient

Sample ID	Roughness (nm)	RMS (nm)	Kurtosis	Skewness	Height(nm)
As deposited	6.1	7.9	0.90	4.5	21.4
150 °C/Vacuum	2.3	2.9	3.14	0.4	7.1
300 °C/Vacuum	2.0	2.5	3.09	0.3	7.7
150 °C/Ar:O_2	2.0	2.7	9.90	1.9	4.9
300 °C/ Ar:O_2	3.7	5.0	29.6	2.2	11.4

increase in temperature for films thermally treated in vacuum. However, a mixed trend in surface roughness evolution was observed for films thermally treated in argon–oxygen ambient. The average transmittance decreased with increase in temperature for films thermally treated in vacuum and increased with temperatures for the films treated in argon–oxygen ambient as the result of improved crystallinity and transformation of surface Cr metal into chromium oxide, respectively. Findings from this study suggest that high temperature and argon–oxygen needed for the deposition of dielectric during deposition of Cr-based multilayer spectral selective films can significantly influence the structure and optical properties of the prior deposited Cr. Therefore, it is essential to consider these changes when designing and depositing multi-layered Cr spectral selective solar absorber films.
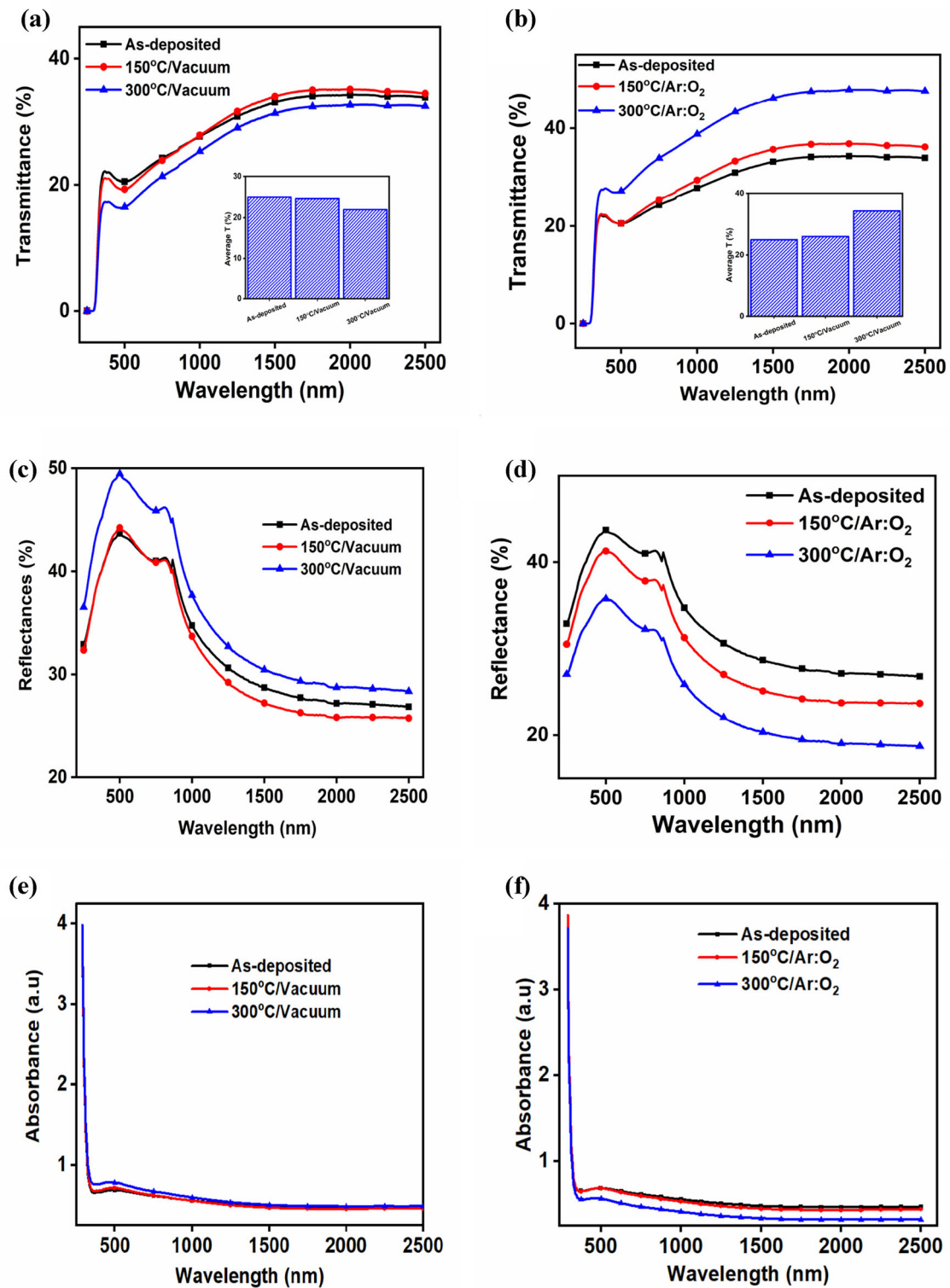
Fig. 10 Optical transmittances, reflectance and absorbance of Cr thin films thermally treated at different temperatures in vacuum (**a**, **c**, **e**) and argon/oxygen ambient (**b**, **d**, **f**)
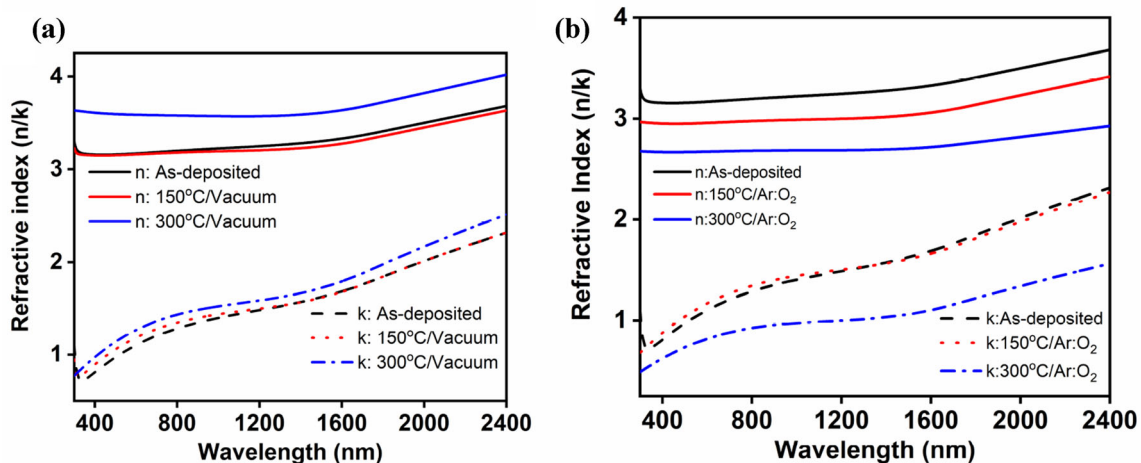
Fig. 11 Refractive index of Cr thin films treated at different temperatures in Vacuum (**a**) and Ar: O_2 ambient (**b**)

Author contributions

All authors contributed to the study conceptualization. Sample preparation, data collection and analysis were performed by JJT. JSN was involved in SEM, Raman and XRD characterization. NRM, MD and MES were involved in financial acquisition and supervision of work. The first draft of the manuscript was written by JJT and all authors reviewed and edited on previous versions of the manuscript. All authors read and approved the final manuscript.

Data availability

The datasets generated during and/or analyzed during the current study are available from the corresponding author on reasonable request.

Declarations

Conflict of interest The authors declare no conflict of interest.

References

1. R.T. Kivaisi, L. Stensland, Appl. Phys. A (1982). https://doi.org/10.1007/BF00619084
2. G. Katumba, J. Lu, L. Olumekor, G. Westin, E. Wäckelgård, J. Sol.-Gel Sci. Technol. (2005). https://doi.org/10.1007/s10971-005-4793-4
3. T.K. Tsai, S.J. Hsueh, J.H. Lee, J.S. Fang, J. Electron. Mater. (2012). https://doi.org/10.1007/s11664-011-1746-2
4. Y. Li, C. Lin, D. Zhou, Y. An, D. Li, C. Chi, H. Huang, S. Yang, C.Y. Tso, C.Y. Chao, B. Huang, Nano Energy (2019). https://doi.org/10.1016/j.nanoen.2019.103947

5. K. Xu, M. Du, L. Hao, J. Mi, Q. Yu, S. Li, J. Materiom. (2020). https://doi.org/10.1016/j.jmat.2019.12.012

6. A. Foroughi-Abari, C. Xu, K.C. Cadien, Thin Solid Films (2012). https://doi.org/10.1016/j.tsf.2011.08.063

7. A. Rauf, K. Ahmed, F. Nasim, A.N. Khan, A. Gul, I.O.P. Conf, Ser. Mater. Sci. Eng. (2016). https://doi.org/10.1088/1757-899X/146/1/012013

8. J. Peralta, J. Esteve, A. Lousa, Thin Solid Films (2020). https://doi.org/10.1016/j.tsf.2019.137676

9. Z.Y. Nuru, M. Msimanga, T.F.G. Muller, C.J. Arendse, C. Mtshali, M. Maaza, Sol. Energy (2015). https://doi.org/10.1016/j.solener.2014.11

10. A.B. Khelifa, S. Khamlich, Z.Y. Nuru, L. Kotsedi, A. Mebrahtu, M. Balgouthi, A.A. Guizani, W. Dimassi, M. Maaza, J. Alloys Compds. (2018). https://doi.org/10.1016/j.jallcom.2017.11.036

11. Z. Zeng, L. Wang, L. Chen, J. Zhang, Surf. Coat. Technol. (2006). https://doi.org/10.1016/j.surfcoat.2006.03.038

12. X.Z. Wang, H.Q. Fan, T. Muneshwar, K. Cadien, J.L. Luo, J. Mater. Sci. Technol. (2021). https://doi.org/10.1016/j.jmst.2020.06.012

13. H. Barshilia, N. Selvakumar, K. Rajam, A. Biswas, J. Appl. Phys. (2008). https://doi.org/10.1063/1.2831364

14. S.F. Wang, H.C. Lin, H.Y. Bor, Y.L. Tsai, C.N. Wei, J. Alloys Compds. (2011). https://doi.org/10.1016/j.jallcom.2011.08.052

15. J.J. Tibaijuka, M.E. Samiji, M. Diale, N.R. Mlyuka, Tanz. J. Sci. (2022). https://doi.org/10.4314/tjs.v48i3.13

16. F. Maury, A. Douard, S. Delclos, D. Samelor, C. Tendero, Surf. Coat. Technol. (2009). https://doi.org/10.1016/j.surfcoat.2009.04.020

17. M. Muralidhar Singh, G. Vijaya, M.S. Krupashankara, B.K. Sridhara, T.N. Shridhar, Mater. Today: Proc. **5**, 2696 (2018). https://doi.org/10.1016/j.matpr.2018.01.050

18. N.R. Mlyuka, PhD Thesis, University of Dar es Salaam (2010)

19. E.R. Ollotu, N.R. Mlyuka, M.E. Samiji, Tanz. J. Sci. (2021). https://doi.org/10.4314/tjs.v47i2

20. N.R. Moody, D.P. Adams, A.A. Volinsky, M.D. Kriese, W.W. Gerberich, Mater. Res. Soc. Symp. Proc. (1999). https://doi.org/10.1557/PROC-586-195

21. R.T. Kivaisi, Sol. Energy Mater. (1981). https://doi.org/10.1016/0165-1633(81)90023-X

22. R.A. Miller, E. Carl, Lowell (1982). https://doi.org/10.1016/0040-6090(82)90019-0

23. C.T. Rueden, J. Schindelin, M.C. Hiner, B.E. DeZonia, A.E. Walter, E.T. Arena, K.W. Eliceiri, BMC Bioinform. (2017). https://doi.org/10.1186/s12859-017-1934-z

24. I. Horcas, R. Fernández, J.M. Gómez-Rodríguez, J. Colchero, J. Gómez-Herrero, A.M. Baro, Rev. Sci. Instrum. (2007). https://doi.org/10.1063/1.2432410h

25. F.D. Hardcastle, I.E. Wachs, J. Mol. Catal. (1988). https://doi.org/10.1016/0304-5102(88)85092-2

26. A.K. Yadav, P. Singh, RSC Adv. (2015). https://doi.org/10.1039/c0xx00000x

27. A. Kumar, D. Pednekar, S. Mukherjee, R.K. Choubey, J. Mater. Sci.: Mater. Electron. (2020). https://doi.org/10.1007/s10854-020-04263-0

28. B. Hymavathi, B. Rajesh Kumar, T. Subba Rao, J. Electron. Mater. (2017). https://doi.org/10.1007/s11664-017-5799-8

29. J.J. Tibaijuka, M.E. Samiji, N.R. Mlyuka, Tanz. J. Sci. **48**, 660 (2018)

30. D. Naveena, T. Logu, K. Sethuraman, A. Chandra Bose, J. Alloys Compds. (2019). https://doi.org/10.1016/j.jallcom.2019.04

31. S. Baturay, A. Tombak, D. Kaya, Y.S. Ocak, M. Tokus, M. Aydemir, T. Kilicoglu, J. Sol-Gel Sci. Technol. (2016). https://doi.org/10.1007/s10971-015-3953-4

32. A. Kumar, M. Kumar, V. Bhatt, S. Mukherjee, S. Kumar, H. Sharma, M.K. Yadav, S. Tomar, J. Yun, R.K. Choubey, Sens. Actuator A Phys. (2021). https://doi.org/10.1016/j.sna.2021.112988

33. M. Hezam, N. Tabet, A. Mekki, Thin Solid Films (2010). https://doi.org/10.1016/j.tsf.2010.03.091

34. G.P. Daniel, V.B. Justinvictor, P.B. Nair, K. Joy, P. Koshy, P.V. Thomas, Phys. B Condens. Matter. (2010). https://doi.org/10.1016/j.physb.2010.01.039

35. P. Eaton, P. West, *Atomic Force Microscopy*, 1st edn. (Oxford University Press, Oxford, 2010), pp.104–121

36. O. Malik, F.J. De la Hidalga-Wade, J. Mater. Res. (2015). https://doi.org/10.1557/jmr.2015.159

37. E.R. Ollotu, J.S. Nyarige, N.R. Mlyuka, M.E. Samiji, M. Diale, J. Mater. Sci. Mater. Electron. (2020). https://doi.org/10.1007/s10854-020-04192-y

38. K.H. Choi, J.Y. Kim, Y.S. Lee, H.J. Kim, Thin Solid Films (1999). https://doi.org/10.1016/S0040-6090(98)01556-9